

Correlation between Structural Changes and Electrical Transport Properties of Spinel ZnFe₂O₄ Nanoparticles under High Pressure

Junkai Zhang,[†] Yilin Zhang,[†] Xiaoxin Wu,[†] Yanzhang Ma,[‡] Su-Ying Chien,[§] Renquan Guan,[†] Dongzhou Zhang,^{||} Bin Yang,[⊥] Bingmin Yan,^{*,#} and Jinghai Yang^{*,†}

HPSTAR
652-2018

[†]Key Laboratory of Functional Materials Physics and Chemistry of the Ministry of Education, Jilin Normal University, Siping 136000, P. R. China

[‡]Department of Mechanical Engineering, Texas Tech University, Lubbock, Texas 79409, United States

[§]College of Science, National Cheng Kung University, Tainan 701, Taiwan

^{||}Hawai'i Institute of Geophysics and Planetology, School of Ocean and Earth Science and Technology, University of Hawai'i at Manoa, Honolulu, Hawaii 96822, United States

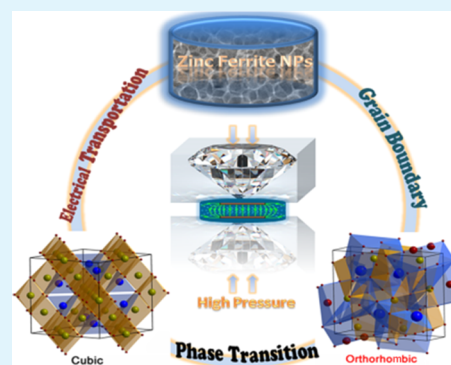
[⊥]Center for High Pressure Science and Technology Advanced Research, Changchun 130012, P. R. China

[#]Center for High Pressure Science and Technology Advanced Research, Beijing 100094, P. R. China

Supporting Information

ABSTRACT: The structural phase transition of synthetic ZnFe₂O₄ nanoparticles (ZFO NPs) is investigated as a function of pressure up to 40.6 GPa at room temperature for the first time, and its associated intriguing electrical transport properties are resolved from in situ impedance spectra and magnetoresistivity measurements. Significant anomalies are observed in the properties of the grain boundary resistance (R_{gb}), the relaxation frequency (f_{max}), and the relative permittivity (ϵ_r) in the ZFO NPs under the pressures around 17.5–21.5 GPa. These anomalies are believed to be correlated with a cubic-to-orthorhombic phase transition of ZnFe₂O₄ at the pressures between 21.9 and 25.7 GPa, which is found to be partially reversible. The pressure-tuned dielectric properties are measured for the cubic and the orthorhombic phases of ZFO, respectively. Remarkably, R_{gb} decreases up to 6 orders of magnitude as a function of pressure in the cubic phase. The dielectric polarization is obviously strengthened with increased f_{max} and decreased ϵ_r with pressure in the orthorhombic phase. Furthermore, it is confirmed that the external pressure effectively improves the electrochemical stability of the sample based on the cycled measurements of the impedance spectra at various pressures. The changes in the complex permittivity (ϵ' , ϵ'') and the dielectric loss tangent ($\tan \delta$) with frequency reveal the irreversible increase in the dielectric loss accompanied by phase transition. The MR measurements indicate that ZFO NPs are superparamagnetic under high pressure of up to 40 GPa. The transmission electron microscopy images reflect the decrease in the grain boundary number and some local amorphization of grains after compression, which provides good explanations for the changes in the electrical transport properties as a function of pressure. Herein, the structural and electrical properties of ZnFe₂O₄ NPs generated are preserved by quenching the high-pressure phase to ambient conditions, thus providing great choices of ferrites materials for a variety of applications.

KEYWORDS: high pressure, spinel ferrite, phase transition, electrical transport properties, grain boundary



INTRODUCTION

Spinel-structured MFe₂O₄ (M = Zn, Cu, Ni, Co, Fe, etc.) ferrites nanomaterials have been among the most popular candidates for studying nanomagnetism due to their great potentials in the wide range of applications from information storage and electronic devices to medical diagnostics and drug delivery.^{1–4} In addition, they are often used for microwave- and radar-absorbing materials due to their high dielectric loss,^{5,6} for supercapacitor as an energy storage/delivery device with good electrochemical properties,^{7,8} and for the anode of

lithium-ion batteries due to their high specific capacity and low cost.^{9–11}

MFe₂O₄ ferrites nanomaterials usually form and stabilize in the cubic spinel structure ($Fd\bar{3}m$) at ambient conditions. The structural formula is generally expressed with $(MFe)_x[MF\bar{e}]_{2-x}O_4$, where round and square brackets denote sites of tetrahedral (A) coordination and octahedral [B]

Received: September 3, 2018

Accepted: November 15, 2018

Published: November 15, 2018

coordination, respectively, and x represents the degree of inversion (i.e., the fraction of the A sites occupied by Fe^{3+}).¹² Considerable studies revealed that the developments of different structures, various morphologies, and compositions result in largely enhanced physical properties and chemical stabilities of MFe_2O_4 nanomaterials. For example, Ju et al.¹³ selectively prepared the cubic and tetragonal CuFe_2O_4 nanoparticles through a method of a facile one-step solid-state reaction route. The cubic CuFe_2O_4 NPs (as anode materials for high power lithium-ion batteries) reveal characteristics such as superior discharge capacity, better cycling performance, and higher rate capability. Furthermore, the morphologies of the cubic MFe_2O_4 ($M = \text{Zn}, \text{Cu}, \text{Ni}, \text{Co}, \text{Fe}$, etc.) nanomaterials can be fabricated in a wide variety of forms for different applications, such as $\text{Co}_3\text{O}_4/\text{ZnFe}_2\text{O}_4$ (ZFO) hollow nanocomposite⁸ for supercapacitor, CuFe_2O_4 nanofibers,¹⁴ CoFe_2O_4 , and NiFe_2O_4 porous ball-in-ball hollow spheres¹⁵ for lithium-ion batteries, as well as ZnFe_2O_4 hollow nanospheres¹⁶ for potential microwave absorber.

Pressure, like temperature and chemical constituent, is one of the most primary factors to radically tune the crystallographic and the microstructural properties (such as morphology, size, grain/grain boundary, defect, etc.), creating a variety of new characteristics. Recent reports indicated that spinel-structured nanomaterials can effectively support the strain caused by the volume change during charge and/or discharge process to alleviate the pulverization problem, coupled with improved electron and Li^+ conduction.¹⁷ Thus, the combination of high-pressure (HP) technique and nanostructuring is expected to provide a new route for modulating the properties of MFe_2O_4 materials.

The high-pressure properties of spinel ferrites originally attract significant interests due to their abundance in the Earth's crust and mantle. There have been several high-pressure structural studies of the spinel ferrite minerals: MgFe_2O_4 ,¹⁸ ZnFe_2O_4 ,¹⁹ CoFe_2O_4 ,²⁰ Fe_3O_4 ,^{21,22} etc., where the equation of state and other mechanical properties, like elastic moduli, have been broadly reported and the denser high-pressure orthorhombic postspinel structure has been revealed. With the development and applications of synthetic MFe_2O_4 materials for various fields, more and more attentions are focused on the field of high-pressure research. Blasco et al.^{22,23} performed high-pressure angle-dispersive X-ray diffraction (XRD) measurements on synthetic $\text{Co}_x\text{Fe}_{3-x}\text{O}_4$ ($x = 0, 1, 1.5, 1.75, 2$) ferrites and observed an irreversible structural phase transformation from the cubic spinel phase to the analogous orthorhombic postspinel phase at pressures around 20 GPa. Ye et al.²⁴ found that MnFe_2O_4 ferrites undergo a phase transition at pressures about 18 GPa to form a denser antiferromagnetic CaMn_2O_4 -type phase, which is stable up to 39.6 GPa and retains its high-pressure polymorph after decompression. Very recently, $\text{Zn}_{0.2}\text{Mg}_{0.8}\text{Fe}_2\text{O}_4$, an intermediate compound with the co-substitution of metal divalent cations, was found to undergo a pressure-induced structural phase transition to an orthorhombic phase (CaTi_2O_4 type, space group $Bbmm$) at pressures of about 21 GPa.²⁵

In addition, nanocrystalline materials have a well-known different high-pressure behavior compared to bulk materials due to the quantum size effect, especially the transition pressure, the structural transformation sequence, and the transportation properties. Although great efforts have been made in studying the crystallography, the electronic structures, and the vibration properties of the bulk MFe_2O_4 ferrites under

high pressure, it seems that structural evolution and properties changes of the nanoscaled MFe_2O_4 are still unclear. For example, Wu et al.²⁶ carried out high-pressure resistance measurements on CoFe_2O_4 NPs and proposed that the phase transition to the postspinel structure occurs at 7.5 and 12 GPa for 80 and 6 nm particles, respectively. The reduction in transition-pressure from 20 to 27 GPa to less than 12 GPa was explained as a consequence of the transformation of CoFe_2O_4 into a metastable phase that does not exist in the bulk material. However, this result conflicts with the known fact that the transition-pressure usually shifts toward higher pressures when reducing the grain size of the nanoparticles.

ZnFe_2O_4 nanoparticles (ZFO NPs), among the most important spinel-structured ferrite nanomaterials, have the characteristics of superparamagnetism and high resistance^{1,27} owing to the small size effect (when the grain size of the NPs is smaller than the critical size of 20 nm). Ferrari et al.²⁸ found that the cubic phase of ZFO NPs (an average grain size of 45 nm) is retained up to 33 GPa, evident by powder X-ray diffraction measurements. Also, a phase transition was induced and an orthorhombic CaMn_2O_4 type phase formed beyond this pressure point. However, this observation is only reported on ZnFe_2O_4 NPs under high pressure so far. The systematic knowledge of the electrical and the magnetic properties of ZnFe_2O_4 nanomaterials at various pressures, especially of ZnFe_2O_4 NPs (size < 20 nm), has not yet been obtained. Therefore, more work is needed to establish a structure–property relationship upon compression. Moreover, pressure-related property changes (such as resistance, dielectric constant, relaxation frequency, energy loss, magnetoresistivity, etc.) also depend on the size changes and the grain boundary effect to a large extent, lack of any of which further prevents the comprehensive understandings of functional ferrites materials under compression.

Motivated by the above-mentioned observations, we conducted the in situ high-pressure angle-dispersive X-ray diffraction experiments, transmission electron microscopy (TEM) measurements, and electrical measurements on ZFO NPs (an average grain size of 9.8 ± 0.1 nm) in this study. First, the XRD spectra of the ZFO NPs under compression were collected to monitor the structural modification, which has not been well-defined yet, providing the basis to understand the pressure-induced property changes. Second, impedance spectra and magnetoresistivity measurements were performed to explore the novel electrical and magnetic properties of ZFO NPs induced by pressure. Last but not the least, TEM measurements were utilized to reveal the changes in the grains/grain boundaries of the ZFO NPs for understanding the variations in the electrical transport properties upon compression.

■ EXPERIMENTAL DETAILS

Sample Preparation. Cubic ZnFe_2O_4 nanoparticles were prepared in the following processes: 0.01 mol $\text{Zn}(\text{Ac})_2 \cdot 2\text{H}_2\text{O}$ and 0.02 mol $\text{Fe}(\text{NO}_3)_3 \cdot 9\text{H}_2\text{O}$ were initially dissolved in 50 mL triethylene glycol inside a reaction vessel and gelled by a catalyst of 0.05 mol trisodium citrate. The solution was heated and continuously stirred at 190 °C until forming a highly viscous gel. Then, the resultant gel was dried in an oven at 60 °C for 24 h. The crystal structure and the microstructure morphologies of the sample were measured at ambient pressure, using XRD with $\lambda = 1.5418$ Å from the Cu $K\alpha$ radiation (Shimadzu XRD-6000), TEM (JEOL 2100), and scanning electron microscopy (SEM) equipped with an energy-dispersive spectrometry (EDS) (JEOL JSM-6700F). Additionally,

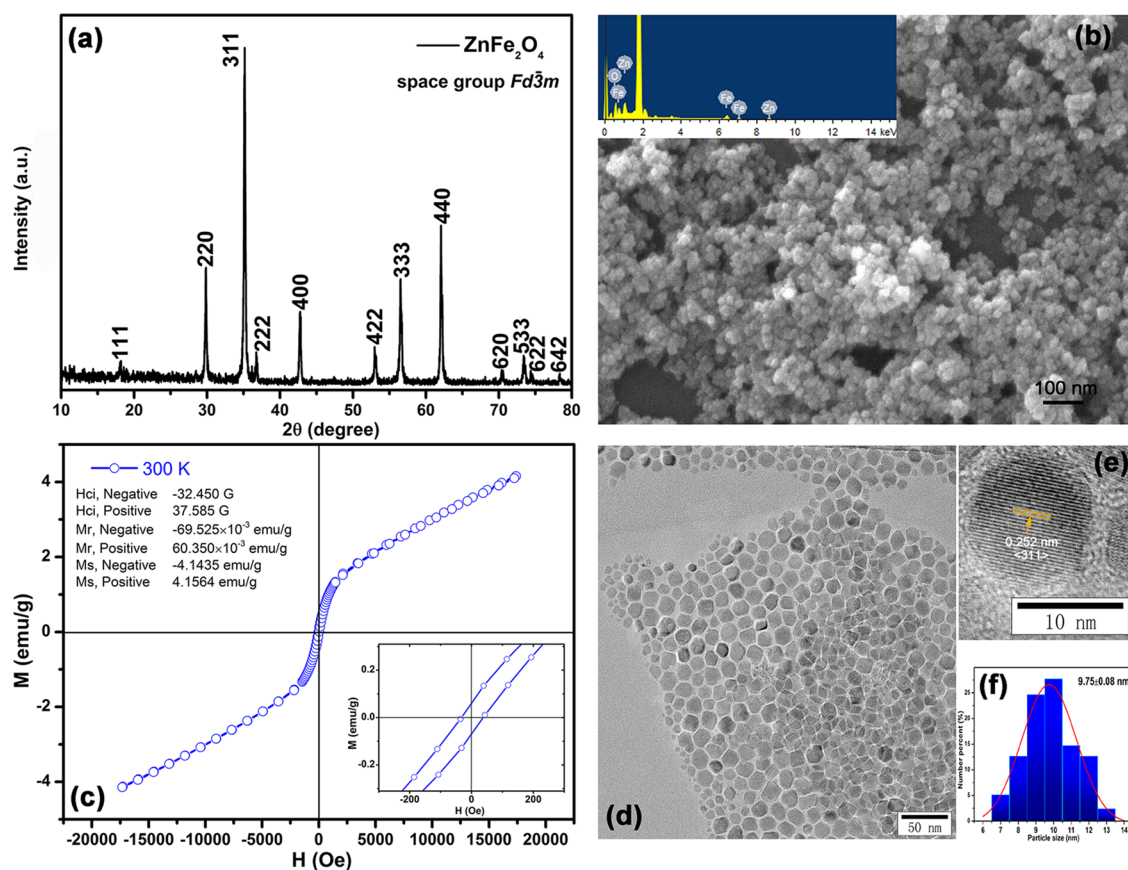


Figure 1. (a) XRD pattern of the as-prepared ZnFe_2O_4 nanoparticles (ZFO NPs) at ambient conditions. All the diffraction peaks in the figure are perfectly indexed as the cubic structure based on the references. (b) SEM image of ZFO NPs and its elemental analysis results determined by EDS. (c) Magnetic hysteresis (M – H) loops of ZFO NPs. (d) TEM image and the corresponding (e) high-resolution transmission electron microscopy (HRTEM) image of ZFO NPs. The $\{311\}$ lattice fringes of the cubic ZnFe_2O_4 are labeled in the HRTEM image. (f) Size distribution of ZFO NPs.

vibrating sample magnetometer (VSM) (LakeShore 7407) was used to measure the magnetic hysteresis (M – H) loops of the sample at room temperature.

In Situ High-Pressure Angle-Dispersive XRD Measurements.

A symmetrical diamond anvil cell (DAC) with a pair of diamond anvils with 300 μm culet size was employed to generate high pressure. A T301 steel gasket was preindented to 40 μm in thickness and a hole with a 150 μm diameter was drilled at the center of the dent as the sample chamber for high-pressure XRD experiments. Powder sample and a small ruby ball were placed into the sample chamber and the in situ pressure was gauged by the R_1 ruby fluorescence method. Silicon oil was used as the pressure-transmitting medium. The schematic drawing of the sample assembly for high-pressure angle-dispersive XRD measurements is further shown in Figure S1 as the Supporting Information. The high-pressure XRD experiments were conducted at the 13-BM-C station of Advanced Photon Source (APS), Argonne National Laboratory (ANL) ($\lambda = 0.406750 \text{ \AA}$). Experimental parameters including the distance between the sample and the detector were calibrated using the CeO_2 standard materials. The two-dimensional (2D) XRD images were induced into the format of intensity versus diffraction angle (2θ) through the integration via the FIT2D program.

In Situ High-Pressure Electrical Measurements. High pressure was generated using a nonmagnetic DAC with a culet size of 400 μm diameter. A nonmagnetic rhenium sheet, used as the gasket, was preindented to 50 μm thickness. A hole 200 μm in diameter was drilled at the center of the indentation using a laser. Then, a mixture of alumina powder and epoxy was inserted and compressed into the hole as the insulating layer. Subsequently, another hole 150 μm in diameter was drilled and served as the sample chamber. The thickness of the sample under high pressure was determined using a micrometer

with a precision of 0.5 μm . No pressure medium was loaded to avoid additional errors in electrical measurements. Ruby fluorescence method was used for the pressure calibration. Parallel-plate capacitor electrodes and van der Pauw configuration electrodes were integrated on the diamond culets for in situ high-pressure impedance spectra and magnetoresistivity measurements, respectively, as shown in Figure S2. The fabricated details of different microcircuits probes on diamond have been reported previously.^{29–31} Impedance spectrum was obtained using a computer-controlled impedance analyzer (Solartron 1260), combined with a dielectric interface (Solartron 1296). A voltage signal with an amplitude of 2 V, and frequency ranging from 10^{-2} to 10^7 Hz was applied to the sample. The magnetoresistivity measurements were conducted using the current reversal method to avoid thermoelectric offsets. The current, typically 100 mA, was sourced by a Keithley 2400 Source Meter and the voltage was measured using a Keithley 2700 Multimeter. A uniform magnetic field with a maximum value of 20 kG was produced by the EM7 electromagnet (East Changing Co.) and exported through two magnetic heads 76 mm in diameter.

DISCUSSION AND RESULTS

As shown in Figure 1a, the XRD result indicates that ZFO NPs crystallize in a cubic structure (space group $Fd\bar{3}m$) at ambient conditions, in agreement with the references.^{11,12,14} Figure 1b,d demonstrates the stoichiometry and the morphology of the ZFO NPs and reveals a uniform size distribution (good dispersibility), as indicated in Figure 1f, which shows an average grain size of $9.8 \pm 0.1 \text{ nm}$. The EDS result, as shown in the inset of Figure 1b, confirms that the sample consists mainly of zinc, iron, and oxygen. In Figure 1c, the M – H loops clearly

show the characteristics of superparamagnetism in ZFO NPs at room temperature (300 K). Our observation is consistent with the literatures.^{1,27} Furthermore, the block temperature (T_B) of ZFO NPs is found to be ~ 35.3 K by using the temperature-dependent magnetic moment measurements under field cooling (FC) and zero field cooling (ZFC) conditions at 500 Oe magnetic field (shown in Figure S3 in the Supporting Information). The block temperature of ZFO NPs is much higher than that ($T_B \sim 9$ K) of bulk ZnFe_2O_4 reported in previous literature,³² which results from strong superexchange interactions between the Fe^{3+} -occupied A sites and Fe^{3+} -occupied B sites in ZFO NPs.

In situ high-pressure XRD measurements were carried out to monitor the structural modification of ZFO NPs upon compression. Figure 2a represents the selected XRD patterns at various pressures at room temperature. We find no considerable changes in the diffraction peaks below 21.9 GPa, except that the peaks gradually shift toward high angles. However, four new diffraction peaks at ~ 9.6 , ~ 10.5 , ~ 14.2 ,

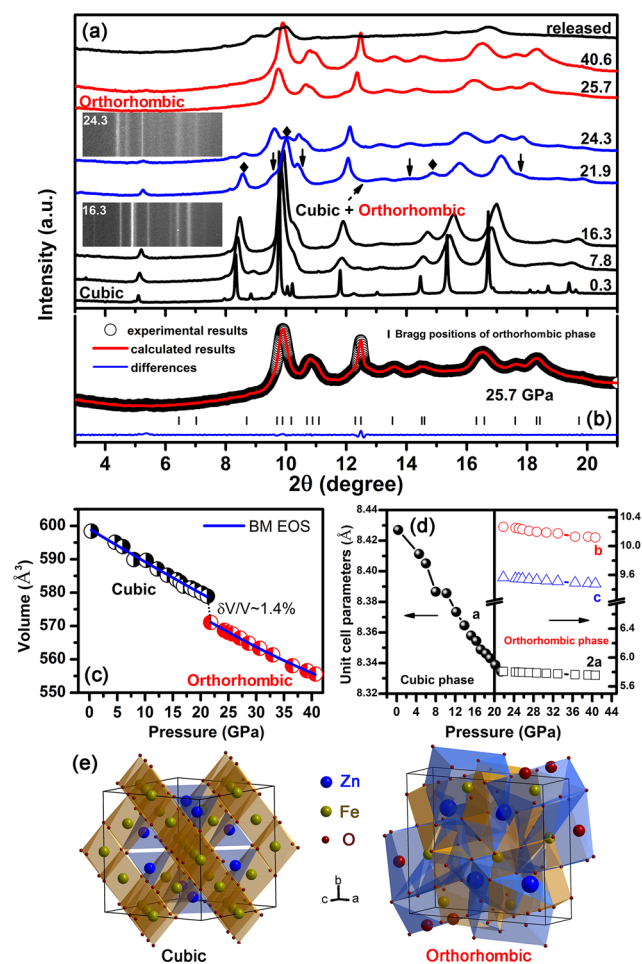


Figure 2. (a) Representative XRD patterns of ZFO NPs at selected pressures at room temperature. The \downarrow symbols point to the emerged new peaks of high-pressure (HP) phase and the \blacklozenge symbols mark the disappearing peaks (significantly reducing in intensity but still observable) of ambient-pressure (AP) phase. (b) Rietveld refinement of the new HP phase at the pressure of 25.7 GPa ($R_w = 1.52\%$ and $R_{wp} = 3.61\%$). (c) Volume and (d) lattice parameters as a function of pressure in the AP and HP phases obtained using XRD and geometry optimization. (e) Schematic structures of ZnFe_2O_4 generated using VESTA.

and $\sim 17.8^\circ$ suddenly emerge as the pressure approaches 21.9 GPa, which clearly signals the start of the structural phase transition. Above 25.7 GPa, the transformation is complete and no further transition is observed up to 40.6 GPa, the highest pressure covered by our experiments. Our observations are consistent with the previous references,^{22–24,26,28} which reported that the cubic spinel ferrites often transform to an HP orthorhombic phase. In Figure 2b, the Rietveld profile fitting at 25.7 GPa further evidences that the best agreement between the observed and calculated patterns is achieved by considering that the new HP phase is the orthorhombic phase. Volume and lattice parameters against pressures are obtained from the fitting results of Rietveld refinements for each diffraction pattern, as shown in Figure 2c,d, respectively. It is found that the pressure-induced cubic-to-orthorhombic phase transition causes an increase in density by approximately 1.4% as a consequence of the volume collapse, on the ZFO nanoparticles. The compressibility is slightly anisotropic in the HP phase. In particular, the *b*-axis is the most compressible one. The structural phase transition involves the rearrangement of atoms in the unit cell. The coordination of cations consequently changes from octahedral and tetrahedral in the cubic phase to octahedral and dodecahedral in the orthorhombic phase,³³ as shown in Figure 2e. Furthermore, upon decompression, we notice that the phase transition is partially reversible.

As clearly shown in Figure 3a, upon quenching to ambient pressure, most of the diffraction peaks of the orthorhombic

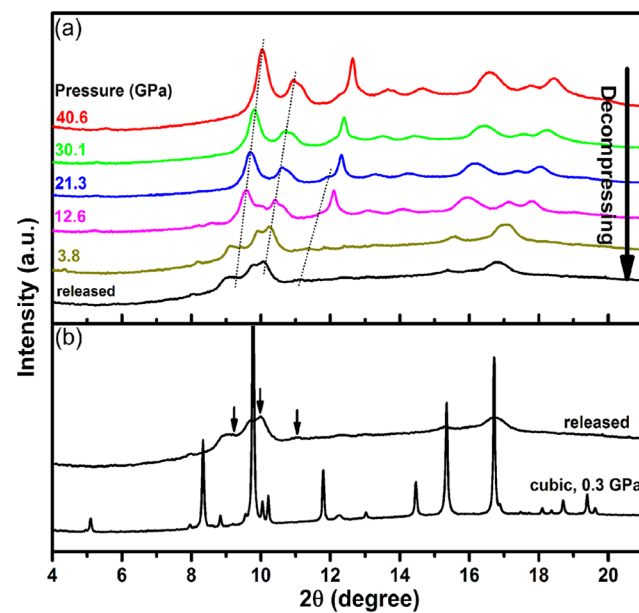


Figure 3. (a) XRD patterns of ZnFe_2O_4 nanoparticles in the decompression run. The dashed lines are guides to the eyes. (b) XRD patterns at 0.3 GPa during compression and after pressure being fully released, respectively. The \downarrow symbols indicate the peaks from the preserved orthorhombic phase.

phase gradually disappear and many diffraction peaks of the cubic phase reappear. When the pressure is fully released, three obvious diffraction peaks of the orthorhombic phase still persist at the 2θ angles marked by the \downarrow symbols in Figure 3b. The sample is found to contain the metastable orthorhombic phase as well as the starting cubic one. It is evident that the structural phase transition is partially reversible.

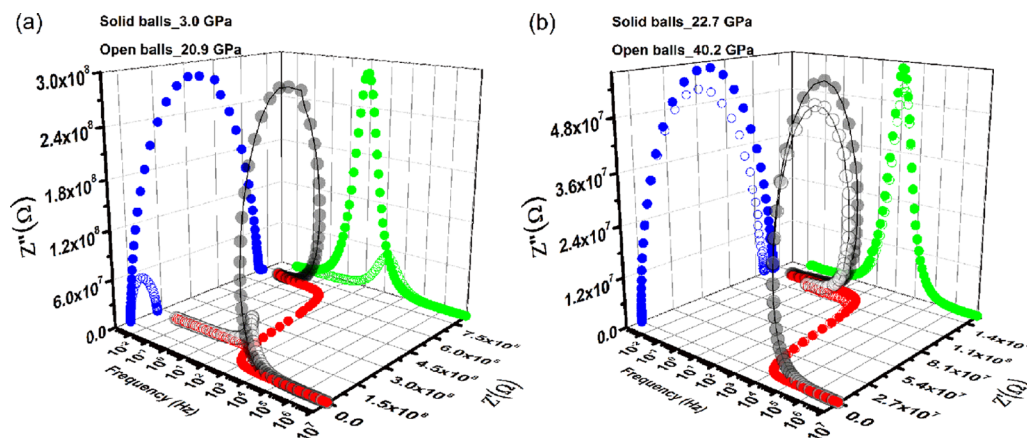


Figure 4. Three-dimensional (3D) impedance spectra (Z' , Z'' , and frequency) of ZFO NPs at (a) 3.0, 20.9, (b) 22.7, and 40.2 GPa under compression, respectively. Gray symbols are 3D curves against Z' , Z'' , and frequency. Blue, green, and red symbols show 2D relationship between Z' and Z'' , Z'' and frequency, and Z' and frequency.

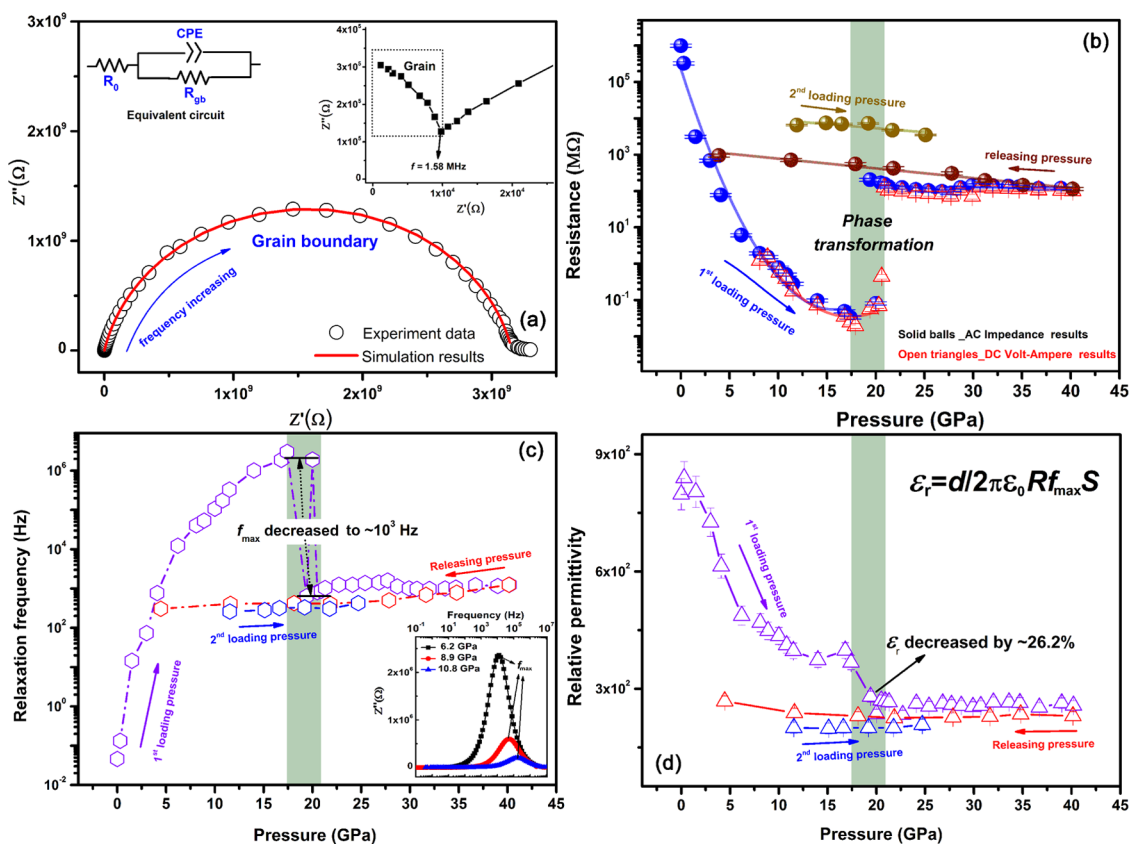


Figure 5. (a) Nyquist plot of impedance spectrum of ZFO NPs at 2.3 GPa with simulation to an RC equivalent circuit. Top-left inset sketches the RC equivalent circuit, where R_{gb} is the grain boundary resistance, CPE is the double-layer capacitance between the sample-to-electrode interfaces, and R_0 is the contact resistance. Top-right inset is the enlarged part of impedance below $2 \times 10^4 \Omega$, which indicates that the required frequency for enhanced grain effect is lower than 1.58×10^6 Hz. Open circles are experimental data and the solid red line is the fitted curve. (b) Cycled pressure dependence of R_{gb} (solid balls). Total resistances (R_{total} , open triangles) obtained from the direct current (DC) volt-ampere measurements are plotted in b for comparison. (c) Cycled pressure dependence of relaxation frequency (f_{max}). Inset is the variation in the imaginary part of impedance as a function of frequency at selected pressures. (d) Cycled pressure dependence of relative permittivity (ϵ_r) obtained according to the formula in the top-right corner. In addition, green bars in (b), (c) and (d) indicate the range of the cubic-to-orthorhombic phase transition.

Discontinuous changes in electrical properties of materials usually coincide with the abrupt structural changes upon compression. Figure 4 illustrates the three-dimensional (3D) perspective plots of impedance spectra of ZFO NPs at selected pressures. Solid and open black lines are the 3D curves, and three 2D projections are shown in the corresponding planes.

The projection to the Z'' and Z' plane is the conventional Nyquist plot of impedance spectrum. Unlike previously reported observations of other bulk materials (such as CdS^{34} and BaTeO_3^{35}) in our previous studies, where two semicircles describing the bulk and grain boundary effect can be clearly distinguished in the Nyquist plots, the Z'' and Z' planes of

ZFO NPs in this study reveal only one complete semicircle at selected pressures. More Nyquist plots of impedance spectra of ZFO NPs under compression are shown in Figure S4. We find out that the contribution from the interior of the grains to the total conductivity of the sample is much weaker than that of grain boundaries, resulting in the difficulty of impedance measurements on the grain effect. In other words, the electrical transport properties of ZnFe_2O_4 ferrite material should be significantly affected by grain boundaries (including the processes of boundary orientation, migration, and reconstruction) in ZFO NPs.

The model of equivalent circuit is generally reliable to demonstrate the impedance behaviors of the powder sample. The parallel resistors (R_{gb}) and constant-phase elements (CPE) in the equivalent circuit model are useful analogues to describe the relaxation process of the grain boundary. In Figure 5a, the experimental impedance data of ZFO NPs are perfectly fitted by a commonly RC equivalent circuit model with the Zview2 software. Besides, the top-right inset in Figure 5a clearly reveals a much smaller contribution from the interior of the grain to the total resistance compared to that of grain boundary at high frequencies above 1.58×10^6 Hz. Similarly, it was found in InN hollow nanotubes³⁶ under compression that the impedance arc of grain interior was covered by that of grain boundaries due to the small size effect and the high interface barrier in nanomaterials. The grain boundary effect was boosted compared to the grain effect and dominant in the total electrical transportation. Hence, the effect on the impedance caused by the interior of grains (bulk resistance) is negligible at frequencies lower than 1.58×10^6 Hz in this study.

The grain boundary resistance (R_{gb}), relaxation frequency (f_{max}), and relative permittivity (ϵ_r) of ZFO NPs are plotted in Figure 5b–d. In AP phase, R_{gb} is about $1 \times 10^{12} \Omega$ at ambient conditions. R_{gb} drops gradually by almost 6 orders of magnitude with increasing pressure up to 17.5 GPa, followed by an abrupt increase between 17.5 and 21.0 GPa (phase transition region). Then, R_{gb} becomes almost P independent (with an average value of $3 \times 10^8 \Omega$) in the orthorhombic phase. R_{total} obtained from the DC volt–ampere measurements further obeys the trend of R_{gb} variations with P (Figure 5b). Furthermore, both f_{max} in Figure 5c and ϵ_r in Figure 5d decrease rapidly by 3 orders of magnitude and by 26.2%, respectively, at the phase transition region (green bars in figures) on loading. In our results, notable anomalies of transportation properties are discovered and correlated with the phase transition. The physics behind this phenomenon is understood as follows: owing to its small size and large specific surface area for nanoparticles, the unsaturated coordinated atoms at grain boundaries are very disordered and the grain boundary barrier is large. The grain boundary effect is dominant in the total electrical transportation. When the cubic-to-orthorhombic phase transition is induced by pressure, the new grain boundaries structure (or rearranging the atoms) is generated. As a consequence, the electrical parameter anomalies are observed during the phase transition. During the decompression after the first loading, R_{gb} increases smoothly and reaches the highest value of $1.2 \times 10^9 \Omega$ at ambient conditions, which is 3 orders of magnitude lower than that of the original state. Upon the cycled decompression, it is found that, all of R_{gb} , f_{max} , and ϵ_r are not fully recovered due to the partial irreversibility of the phase transition and the underlying grain boundary effect. The results show that the ZFO NPs gain

preservable higher stability and lower resistive–dielectric properties after the pressure cycling (loading–releasing–releasing cycle).

To gain a deeper insight into the energy exchange from the dielectric relaxation, the complex permittivity (ϵ' , ϵ'') as a function of frequency (f) and the dielectric loss factor ($\tan \delta$) as a function of $\log f$ under various pressures are investigated in ZFO NPs, as shown in Figure 6. An undispersive characteristic

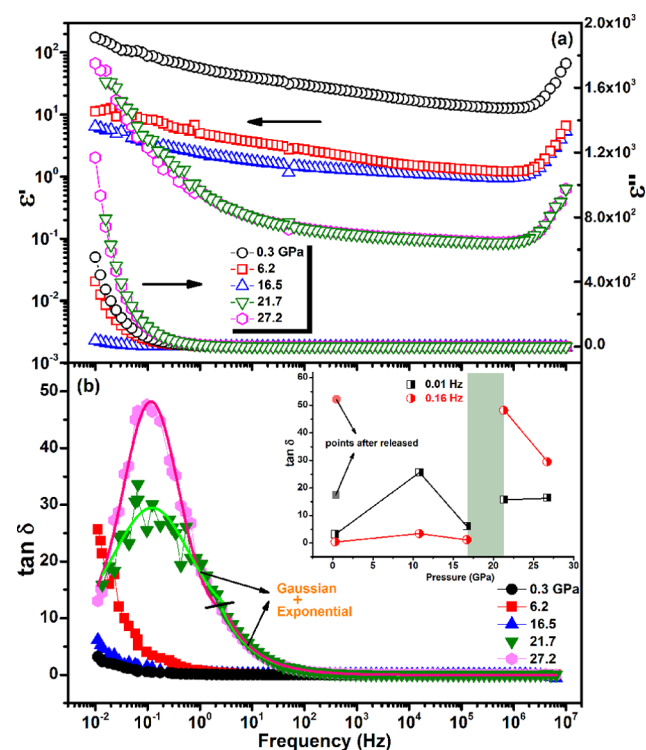


Figure 6. Frequency dependences of (a) complex permittivity (ϵ' , ϵ'') and (b) dielectric loss factor ($\tan \delta$) of ZFO NPs at representative pressures. Inset of (b) shows the plots of $\tan \delta$ at relative low frequencies of 0.01 and 0.16 Hz, respectively, as a function of pressure.

of dielectric relaxation is found (Figure 6a). The ϵ' decreases gradually with increasing f below 1×10^6 Hz, which is mainly caused due to two reasons: the suppression of the orientation of dipoles as the applied field increases with shorter oscillating period; and the number of dipoles contributing to the polarization decreasing with f . But, when subjected to higher frequencies above 1×10^6 Hz, ϵ' turns to increase with f . This often occurs in the heterogeneous systems in which the component dielectrics have different conductivities, i.e., the $f > 1 \times 10^6$ Hz region emerges with the gradual transformation from the grain boundaries dominant to the grain interiors dominant during the relaxation processes. On the other hand, the imaginary part of permittivity (ϵ'') is dramatically reduced with increasing f up to 1 Hz, followed by ϵ'' being independent of f , indicating the coexistence of the conductive loss and the dielectric relaxation loss in the dielectric relaxation. Furthermore, the mean magnitude of ϵ' within the full frequency region decreases during the structural phase transition of ZFO NPs, accompanied by simultaneous increase in ϵ'' , indicating the redshift of undispersive region toward the higher frequencies due to the application of pressure.

The value of $\tan \delta$ is the ratio of the energy dissipation of material to the energy storage over a period of time. In Figure 6b, $\tan \delta$ appears as the strongest dissipation peak between 1×10^{-2} and 1×10^7 Hz above 21.7 GPa, which is well simulated using a two-piece nonlinear fitting. By fitting the data, we obtain two representative values of $\tan \delta$ being 0.01 and 0.16 Hz, respectively (inset of Figure 6b). It is found that a higher dielectric loss is produced during the cubic-to-orthorhombic phase transition and indeed it cannot be recovered to the initial state after the pressure is fully released. Therefore, the absorption properties of ZnFe_2O_4 ferrite nanomaterials can be improved, as expected, by the use of modulating the crystalline and the electronic structures induced by the external pressure.

For achieving the spin-polarized hopping of localized carriers through the presence of the magnetic disorder and the pressure dependence, the magnetoresistivity (MR) as a function of magnetic field (B) of ZFO NPs is measured at different pressures, as shown in Figure 7. The magnetoresistivity is

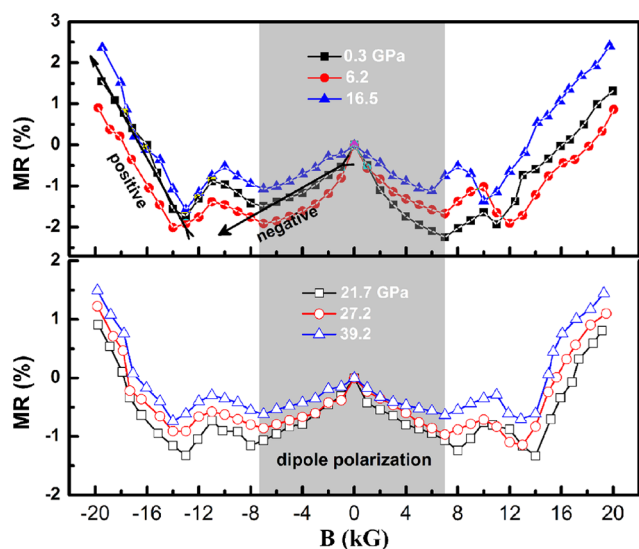


Figure 7. Magnetoresistivity (MR) versus magnetic field (B) curves of ZFO NPs at selected pressures with a magnetic field applied perpendicular to the sample chamber. Arrows in the upper half of the figure are the guides for the eyes.

defined as $\text{MR} = [\rho(H) - \rho(0)]/\rho(0)$, where $\rho(H)$ and $\rho(0)$ are the resistivity with and without the parallel magnetic field, respectively. For $(\text{ZnFe})_x[\text{ZnFe}]_{2-x}\text{O}_4$, the nonmagnetic Zn^{2+} prefers to occupy the [A] sites but also displaces some Fe^{3+} from (B) to [A] sites. Thus, the disordering of the cations enhances the superexchange interaction of A–O–B, exhibiting the characteristic of spins canting. Further, the enhanced spin canting enlarges the scattering of the carriers and results in a higher electrical resistivity in the sample without the applied magnetic field ($B = 0$ Gauss). Upon increasing B , the angle of spin canting reduces, and consequently the electrical conduction increases. Therefore, it is expected that the curves of MR vs B show a decreasing trend at a relatively low B with the characteristic of the anomalous magnetic resistance. But when subjected to the higher B over 7 kG, MR is observed to increase with further increase in B , with the characteristic of the Ordinary Magnetoresistivity (OMR). This is ascribed as the consequence of the lengthened electrons transport path and the increased probability for the electron collision due to the Hall effect under different B . In addition, the variation in MR with B is found to be rarely affected by the application of pressure, except for the differences in the magnitude of the reduction at $B = 7$ kG, indicating that ZFO NPs keep its superparamagnetism under high-pressure loading.

Figure 8 shows the HRTEM measurements of the ZnFe_2O_4 sample that was quenched from 2.8, 16.7, and 22.3 GPa, respectively. It is found that the number of grain boundaries is reduced with significant decrease in the number of grains upon compression from 2.8 to 16.7 to 22.3 GPa. It shows the ability to weaken the scattering of carriers and coincides with the decreasing of R_{gb} with pressure. Furthermore, the local grains are found to become amorphous in the quenched sample and hence the percentage of unsaturated atoms at grain boundaries becomes low. The capacity of charge bonding is reduced with respect to the dangling bonds with pressure, which is likely to be cause for the continuous decrease in ϵ_r upon compression. In addition, the irreversibility of grain boundaries after the pressure is fully released is also a key factor to influence the pressure-tuning of the electrical transport properties of ZFO NPs.

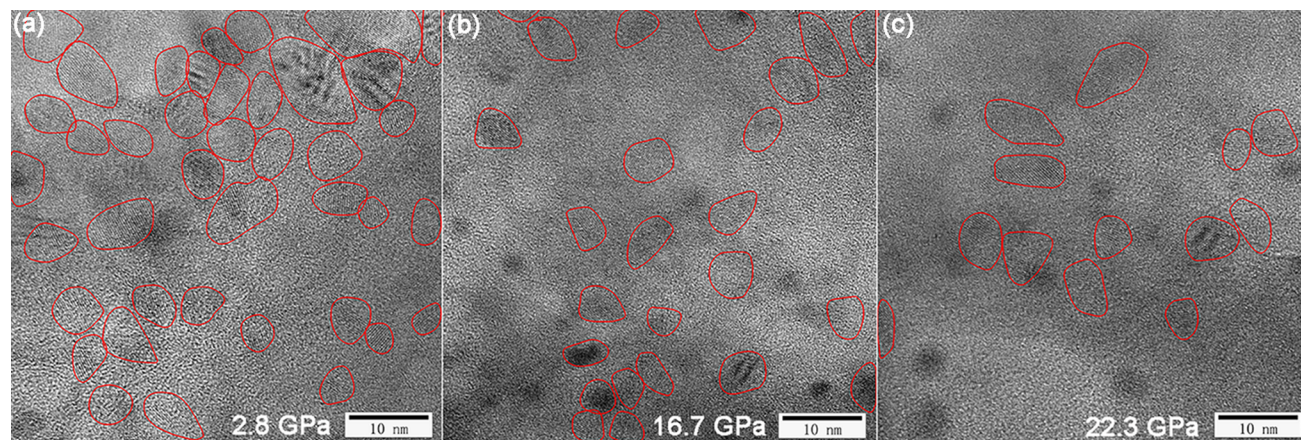


Figure 8. High-resolution transmission electron microscopy (HRTEM) images of ZFO NPs quenched from selected pressures: 2.8 GPa (a), 16.7 GPa (b), and 22.3 GPa (c), respectively. Grains are marked by red circles.

CONCLUSIONS

The effects of pressure on both structural phase transition and electrical transport properties of synthetic ZnFe_2O_4 nanoparticles (ZFO NPs) were studied as a function of pressure up to 40.6 GPa at room temperature for the first time. It is evident that ZFO NPs undergo a partially reversible cubic-to-orthorhombic phase transition at pressures between 21.9 and 25.7 GPa. This structural transformation correlates with notable anomalies of R_{gb} , f_{max} and ϵ_r within the pressure range of 17.5–21.5 GPa. Our results show that R_{gb} , f_{max} and ϵ_r changes dramatically in the cubic phase than in the orthorhombic phase with increasing pressure. The dielectric polarization is enhanced by increasing f_{max} and decreasing ϵ_r with pressures. Additionally, the existence of external pressure improves the electrochemical stability of the sample. The behavior of higher dielectric loss is retained from the phase transition. Moreover, the superparamagnetism of ZFO NPs is still measurable under high pressure close to 40 GPa. The reduced grain boundary number and the local amorphization of the grains are found on the TEM images of the quenched sample. After the high-pressure annealing, the high-pressure polymorph (orthorhombic phase) of ZFO NPs can be partially preserved, so do their improved electrical properties. This shows the great potentials of the pressure-treated ferrites materials for a broad range of applications.

ASSOCIATED CONTENT

Supporting Information

The Supporting Information is available free of charge on the ACS Publications website at DOI: 10.1021/acsami.8b15259.

Sample assembly drawing; comparison of van der Pauw model and the parallel-plate capacitor electrodes; temperature-dependent magnetic moment under FC and ZFC conditions; Nyquist plots of impedance spectra and relaxation peaks of grain boundaries under compression (PDF)

AUTHOR INFORMATION

Corresponding Authors

*E-mail: bingmin.yan@hpstar.ac.cn (B.Y.).

*E-mail: jhyang1@jnu.edu.cn (J.Y.).

ORCID

Junkai Zhang: 0000-0002-6407-6173

Notes

The authors declare no competing financial interest.

ACKNOWLEDGMENTS

This work was supported by the National Natural Science Foundation of China (Grant Nos. 11504132, 21878119, 21776110, and 61775081) and the Thirteenth Five-Year Program for Science and Technology of Education Department of Jilin Province (Item No. JJKH20180769KJ). In situ high-pressure XRD experiments were performed at the 13-BM-C of GeoSoilEnviroCARS (The University of Chicago, Sector 13), Advanced Photon Source (APS), and Argonne National Laboratory (ANL). GeoSoilEnviroCARS is supported by the National Science Foundation Earth Sciences (Grant No. EAR-1128799) and Department of Energy-GeoSciences (Grant No. DE-FG02-94ER14466). This research used resources of the Advanced Photon Source, a U.S. DOE Office of Science User Facility operated for the DOE Office of Science by Argonne

National Laboratory under Contract No. DE-AC02-06CH11357.

REFERENCES

- (1) Wang, Y.; Li, L. P.; Zhang, Y. L.; Chen, X. Q.; Fang, S. F.; Li, G. S. Growth Kinetics, Cation Occupancy, and Magnetic Properties of Multimetal Oxide Nanoparticles: A Case Study on Spinel NiFe_2O_4 . *Phys. Chem. C* **2017**, *121*, 19467–19477.
- (2) Antonello, A.; Jakob, G.; Dolcet, P.; Momper, R.; Kokkinopoulou, M.; Landfester, K.; Muñoz-Espí, R.; Gross, S. Synergy of Miniemulsion and Solvothermal Conditions for the Low-Temperature Crystallization of Magnetic Nanostructured Transition-Metal Ferrites. *Chem. Mater.* **2017**, *29*, 985–997.
- (3) Nandwana, V.; Zhou, R. Y.; Mohapatra, J.; Kim, S.; Prasad, P. V.; Liu, J. P.; Dravid, V. P. Exchange Coupling in Soft Magnetic Nanostructures and Its Direct Effect on Their Theranostic Properties. *ACS Appl. Mater. Interfaces* **2018**, *10*, 27233–27243.
- (4) Yin, P. T.; Pongkulapa, T.; Cho, H. -Y.; Han, J. Y.; Pasquale, N. J.; Rabie, H.; Kim, J. -H.; Choi, J. -W.; Lee, K. -B. Overcoming Chemoresistance in Cancer via Combined MicroRNA Therapeutics with Anticancer Drugs Using Multifunctional Magnetic Core-Shell Nanoparticles. *ACS Appl. Mater. Interfaces* **2018**, *10*, 26954–26963.
- (5) Feng, J. T.; Hou, Y. H.; Wang, Y. C.; Li, L. C. Synthesis of Hierarchical $\text{ZnFe}_2\text{O}_4@SiO_2@RGO$ Core-Shell Microspheres for Enhanced Electromagnetic Wave Absorption. *ACS Appl. Mater. Interfaces* **2017**, *9*, 14103–14111.
- (6) Lv, H. L.; Zhang, H. Q.; Ji, G. B.; Xu, Z. J. Interface Strategy To Achieve Tunable High Frequency Attenuation. *ACS Appl. Mater. Interfaces* **2016**, *8*, 6529–6538.
- (7) Young, C.; Kim, J.; Kaneti, Y. V.; Yamauchi, Y. One-Step Synthetic Strategy of Hybrid Materials from Bimetallic Metal-Organic Frameworks for Supercapacitor Applications. *ACS Appl. Energy Mater.* **2018**, *1*, 2007–2015.
- (8) Hu, X.-W.; Liu, S.; Qu, B.-T.; You, X.-Z. Starfish-shaped $\text{Co}_3\text{O}_4/\text{ZnFe}_2\text{O}_4$ Hollow Nanocomposite: Synthesis, Supercapacity, and Magnetic Properties. *ACS Appl. Mater. Interfaces* **2015**, *7*, 9972–9981.
- (9) Zhang, Y. M.; Pelliccione, C. J.; Brady, A. B.; Guo, H. Y.; Smith, P. F.; Liu, P.; Marschilok, A. C.; Takeuchi, K. J.; Takeuchi, E. S. Probing the Li Insertion Mechanism of ZnFe_2O_4 in Li-Ion Batteries: A Combined X-Ray Diffraction, Extended X-Ray Absorption Fine Structure, and Density Functional Theory Study. *Chem. Mater.* **2017**, *29*, 4282–4292.
- (10) Yue, H. Y.; Du, T.; Wang, Q. X.; Shi, Z. P.; Dong, H. Y.; Cao, Z. X.; Qiao, Y.; Yin, Y. H.; Xing, R. M.; Yang, S. T. Biomimetic Synthesis of Polydopamine Coated ZnFe_2O_4 Composites as Anode Materials for Lithium-Ion Batteries. *ACS Omega* **2018**, *3*, 2699–2705.
- (11) Hameed, A. S.; Bahiraei, H.; Reddy, M. V.; Shoushtari, M. Z.; Vittal, J. J.; Ong, C. K.; Chowdari, B. V. R. Lithium Storage Properties of Pristine and (Mg, Cu) Codoped ZnFe_2O_4 Nanoparticles. *ACS Appl. Mater. Interfaces* **2014**, *6*, 10744–10753.
- (12) Hazra, S.; Ghosh, N. N. Preparation of Nanoferrites and Their Applications. *J. Nanosci. Nanotechnol.* **2014**, *14*, 1983–2000.
- (13) Xing, Z.; Ju, Z.; Yang, J.; Xu, H.; Qian, Y. One-step Solid State Reaction to Selectively Fabricate Cubic and Tetragonal CuFe_2O_4 Anode Material for High Power Lithium Ion Batteries. *Electrochim. Acta* **2013**, *102*, 51–57.
- (14) Luo, L.; Cui, R.; Qiao, H.; Chen, K.; Fei, Y.; Li, D.; Pang, Z.; Liu, K.; Wei, Q. High Lithium Electroactivity of Electrospun CuFe_2O_4 Nanofibers as Anode Material for Lithium-ion Batteries. *Electrochim. Acta* **2014**, *144*, 85–91.
- (15) Li, S. L.; Li, A. H.; Zhang, R. R.; He, Y. Y.; Zhai, Y. J.; Xu, L. Q. One-dimensional Manganese Borate Hydroxide Nanorods and the Corresponding Manganese Oxyborate Nanorods as Promising Anodes for Lithium Ion Batteries. *Nano Res.* **2014**, *7*, 1116–1127.
- (16) Yan, A. G.; Liu, X. H.; Yi, R.; Shi, R. R.; Zhang, N.; Qiu, G. Z. Selective Synthesis and Properties of Monodisperse Zn Ferrite Hollow Nanospheres and Nanosheets. *J. Phys. Chem. C* **2008**, *112*, 8558–8563.

- (17) Chen, Y.; Zhu, J.; Qu, B.; Lu, B.; Xu, Z. Graphene Improving Lithium-ion Battery Performance by Construction of NiCo₂O₄/Graphene Hybrid Nanosheet Arrays. *Nano Energy* **2014**, *3*, 88–94.
- (18) Levy, D.; Diella, V.; Dapiaggi, M.; Sani, A.; Gemmi, M.; Pavese, A. Equation of State, Structural Behaviour and Phase Diagram of Synthetic MgFe₂O₄, as a Function of Pressure and Temperature. *Phys. Chem. Min.* **2004**, *31*, 122–129.
- (19) Levy, D.; Pavese, A.; Hanfland, M. Phase Transition of Synthetic Zinc Ferrite Spinel (ZnFe₂O₄) at High Pressure, from Synchrotron X-ray Powder Diffraction. *Phys. Chem. Min.* **2000**, *27*, 638–644.
- (20) Wang, Z.; Downs, R. T.; Pischedda, V.; Shetty, R.; Saxena, S. K.; Zha, C. S.; Zhao, Y. S.; Schiferl, D.; Waskowska, A. High-Pressure X-ray Diffraction and Raman Spectroscopic Studies of the Tetragonal Spinel CoFe₂O₄. *Phys. Rev. B* **2003**, *68*, 094101-1-6.
- (21) Haavik, C.; Stolen, S.; Fjellvag, H.; Hanfland, M.; Huasermann, D. Equation of State of Magnetite and its High-Pressure Modification: Thermodynamics of the Fe-O System at High Pressure. *Am. Min.* **2000**, *85*, 514–523.
- (22) Subías, G.; Cuartero, V.; García, J.; Blasco, J.; Lafuerza, S.; Pascarelli, S.; Mathon, O.; Strohm, C.; Nagai, K.; Mito, M.; Garbarino, G. Investigation of Pressure-Induced Magnetic Transitions in Co_xFe_{3-x}O₄ Spinel. *Phys. Rev. B* **2013**, *87*, No. 094408.
- (23) Blasco, J.; Subías, G.; García, J.; Popescu, C.; Cuartero, V. High-Pressure Transformation in the Cobalt Spinel Ferrites. *J. Solid State Chem.* **2015**, *221*, 173–177.
- (24) Ye, L. J.; Zhai, S. M.; Wu, X.; Xu, C. W.; Yang, K.; Higo, Y. J. Compressibilities of MnFe₂O₄ Polymorphs. *Phys. Chem. Min.* **2015**, *42*, 569–577.
- (25) Rahman, S.; Samanta, S.; Errandonea, D.; Yan, S.; Yang, K.; Lu, J. L.; Wang, L. Pressure-Induced Structural Evaluation and Insulator-Metal Transition in the Mixed Spinel Ferrite Zn_{0.2}Mg_{0.8}Fe₂O₄. *Phys. Rev. B* **2017**, *95*, No. 024107.
- (26) Wu, Z. Y.; Bao, Z. X.; Cao, L.; Liu, C. X.; Li, Q. S.; Xie, S. S.; Zou, B. S. Electrical Properties and Phase Transition of CoFe₂O₄ Nanocrystals under Pressure. *J. Appl. Phys.* **2003**, *93*, 9983–9987.
- (27) Yao, C. W.; Zeng, Q. S.; Goya, G. F.; Torres, T.; Liu, J. F.; Wu, H. P.; Ge, M. Y.; Zeng, Y. W.; Wang, Y. W.; Jiang, J. Z. ZnFe₂O₄ Nanocrystals: Synthesis and Magnetic Properties. *J. Phys. Chem. C* **2007**, *111*, 12274–12278.
- (28) Ferrari, S.; Kumar, R. S.; Grinblat, F.; Apesteguy, J. C.; Saccone, F. D.; Errandonea, D. In situ High-Pressure X-ray Diffraction Study of Zinc Ferrite Nanoparticles. *Solid State Sci.* **2016**, *56*, 68–72.
- (29) Gao, C.; Han, Y.; Ma, Y.; White, A.; Liu, H.; Luo, J.; Li, M.; He, C.; Hao, A.; Huang, X. Accurate Measurements of High Pressure Resistivity in a Diamond Anvil Cell. *Rev. Sci. Instrum.* **2005**, *76*, No. 083912.
- (30) Wang, Q. L.; Liu, C. L.; Han, Y. H.; Gao, C. X.; Ma, Y. Z. The Determination of Ionic Transport Properties at High Pressures in a Diamond Anvil Cell. *Rev. Sci. Instrum.* **2016**, *87*, No. 123904.
- (31) Sang, D. D.; Wang, Q. L.; Zhang, B. Y.; Wang, W. J.; Hu, H. Q. Role of the Grain Boundaries on the Electrical Transport Behavior of Nanocrystalline BaTiO₃ under High Pressure. *Nat. Sci.* **2018**, *31*, 50–55.
- (32) Li, F. S.; Wang, L.; Wang, J. B.; Zhou, Q. G.; Zhou, X. Z.; Kunkel, H. P.; Williams, G. Site Preference of Fe in Nanoparticles of ZnFe₂O₄. *J. Magn. Mater.* **2004**, *268*, 332–339.
- (33) Manjon, F. J.; Tiginyanu, I.; Ursaki, V. *Pressure-Induced Phase Transitions in AB₂X₄ Chalcogenide Compounds*; Springer: Berlin, 2014.
- (34) He, C. Y.; Gao, C. X.; Ma, Y. Z.; Li, M.; Hao, A. M.; Huang, X. W.; Liu, B. G.; Zhang, D. M.; Yu, C. L.; Zou, G. T.; Li, Y. C.; Li, H.; Li, X. D.; Liu, J. In situ Electrical Impedance Spectroscopy under High Pressure on Diamond Anvil Cell. *Appl. Phys. Lett.* **2007**, *91*, No. 092124.
- (35) Li, Y.; Han, Y. H.; Ma, Y. Z.; Zhu, P. W.; Wang, X.; Gao, C. X. Pressure Effects on Grain Boundary, Electrical and Vibrational Properties of the Polycrystalline BaTeO₃. *Europhys. Lett.* **2012**, *98*, No. 66006.
- (36) Zhang, J. K.; Ma, Y. Z.; Sun, M. L.; Yin, G. C.; Yang, J. H. Structural and Electrical Properties of InN Hollow Nanotubes under High Pressure. *Mater. Lett.* **2018**, *213*, 306–310.